HAL
open science

Identification of sources of potential fields with the continuous wavelet transform: Basic theory

Frédérique Moreau, Dominique Gibert, Matthias Holschneider, Ginette Saracco

To cite this version:

Frédérique Moreau, Dominique Gibert, Matthias Holschneider, Ginette Saracco. Identification of sources of potential fields with the continuous wavelet transform: Basic theory. Journal of Geophysical Research : Solid Earth, 1999, 104 (B3), pp.5003 - 5013. 10.1029/1998JB900106 . hal-01767213

HAL Id: hal-01767213

https://hal.science/hal-01767213v1

Submitted on 19 Sep 2019

HAL is a multi-disciplinary open access archive for the deposit and dissemination of scientific research documents, whether they are published or not. The documents may come from teaching and research institutions in France or abroad, or from public or private research centers.

L'archive ouverte pluridisciplinaire **HAL**, est destinée au dépôt et à la diffusion de documents scientifiques de niveau recherche, publiés ou non, émanant des établissements d'enseignement et de recherche français ou étrangers, des laboratoires publics ou privés.

JOURNAL OF GEOPHYSICAL RESEARCH, VOL. 104, NO. B3, PAGES 5003–5013, MARCH 10, 1999

Identification of sources of potential fields with the continuous wavelet transform: Basic theory

Frédérique Moreau and Dominique Gibert

Géosciences Rennes - CNRS/INSU, Université de Rennes 1, Rennes, France

Matthias Holschneider

Centre de Physique Théorique, CNRS Luminy, Marseille, France

Ginette Saracco

Géosciences Rennes - CNRS/INSU, Université de Rennes 1, Rennes, France

Abstract. The continuous wavelet transform is used to analyze potential fields and to locate their causative sources. A particular class of wavelets is introduced which remains invariant under the action of the upward continuation operator in potential field theory. These wavelets make the corresponding wavelet transforms easy to analyze and the sources' parameters (horizontal location, depth, multipolar nature, and strength) simple to estimate. Practical issues (effects of noise, choice of the analyzing wavelet, etc.) are addressed. A field data example corresponding to a near-surface magnetic survey is discussed. Applications to the high-resolution aeromagnetic survey of French Guyana will be discussed in the next paper of the series.

1. Introduction

The recovery of the causative sources of potential fields (e.g., magnetic and gravitational) measured at the surface of the Earth is a long-standing topic, and a number of techniques have been proposed to address the problem of source determination (see *Blakely* [1995] for a review). These techniques roughly fall within two categories: processing or inversion. The latter category concerns the methods for which the main goal is to recover the source distribution responsible for the measured potential field. It is well known that the resulting inverse problems are dramatically ill posed both mathematically and numerically and that practical solutions can be obtained only when reliable a priori constraints can be added to the problem at hand (see *Parker* [1994] and references therein for a general discussion). The methods belonging to the processing family do not transfer the information contained in the data set into the source distribution space, but instead transfer information into auxiliary spaces such as, for instance, the Fourier domain where the information concerning the depth to top of the causative sources is eventually easier to obtain [*Spector and Grant*, 1970; *Green*, 1972]. In the same spirit, transformation methods produce transformed fields (upward continuation; horizontal, vertical, or oblique derivatives; and reduction to the pole) where the desired information is hopefully enhanced [*Gibert and Galdéano*, 1985; *Sowerbutts*, 1987].

The method we propose in this paper follows the processing approach and transfers the original information carried by the data into the wavelet transform space. The wavelet transform presents several advantages with respect to other methods. For instance, it allows a local analysis of the measured field contrary to the global Fourier transform. Also, the wavelet transform provides a mean to correctly handle the noise present in the data, which is not possible so easily with the local Euler deconvolution [*Thompson*, 1982]. These advantages make the wavelet transform attractive for processing potential field data [*Moreau et al.*, 1997; *Hornby et al.*, 1999]. More precisely, we shall show that only a subset of the wavelet transform is sufficient to get the information necessary to identify and characterize the sources producing the observed potential field. This information is obtained from the local homogeneity properties of the measured field by means of the continuous wavelet transform, whose mathematical properties are recalled in section 2.1. Then, a particular class of wavelets is introduced which allows for a remarkable property of the wavelet transform with respect to the harmonic continuation of potential fields. Next, the properties of these wavelets are discussed and illustrated with several synthetic examples. Finally, a simple field example of a magnetic survey is presented.

Copyright 1999 by the American Geophysical Union.

Paper number 1998JB900106.
0148-0227/99/1998JB900106$09.00

2. Mathematical Framework

In this section, only the main mathematical aspects needed to establish the method are presented. A detailed discussion can be found in the paper by *Moreau et al.* [1997].

2.1. The Continuous Wavelet Transform

We define the continuous wavelet transform of a function $\phi_0\,(x \in \mathbb{R}^n)$ as a convolution product,

$$\begin{aligned} \mathcal{W}[g,\phi_0](b,a) &\equiv \int_{\mathbb{R}^n} \mathrm{d}x \frac{1}{a^n} g\left(\frac{b-x}{a}\right)\phi_0(x) \\ &= (\mathcal{D}_a g * \phi_0)(b), \end{aligned} \tag{1}$$

where $g\,(x \in \mathbb{R}^n)$ is the analyzing wavelet, $a \in \mathbb{R}^+$ is the dilation, and the dilation operator $\mathcal{D}_a$ is defined by the following action:

$$\mathcal{D}_a g(x) \equiv \frac{1}{a^n} g\left(\frac{x}{a}\right). \tag{2}$$

The analyzing wavelet may be freely chosen in the class of the oscillating functions having a vanishing integral and whose support may be restricted to a finite interval containing the origin [*Holschneider*, 1995]. Several wavelets are shown in Figure 1. The main mathematical property we need in this paper is the covariance of the wavelet transform with respect to dilation, i.e.,

$$\mathcal{W}[g,\mathcal{D}_\lambda\phi_0](b,a) = \frac{1}{\lambda^n}\mathcal{W}[g,\phi_0]\left(\frac{b}{\lambda},\frac{a}{\lambda}\right). \tag{3}$$

This property implies a remarkable behavior of the wavelet transform of homogeneous functions ϕ_0 of degree $\alpha \in \mathbb{R}$ for which

$$\phi_0(\lambda x) = \lambda^\alpha \phi_0(x) \quad \forall \lambda > 0. \tag{4}$$

Let us recall that the Dirac and Heaviside distributions are homogeneous with $\alpha = -n$ and $\alpha = 0$, respectively. For a function satisfying (4), (3) simplifies to

$$\mathcal{W}[g,\phi_0](\lambda b,\lambda a) = \lambda^\alpha \mathcal{W}[g,\phi_0](b,a), \tag{5}$$

which indicates that the whole wavelet transform of a homogeneous function can be obtained by dilating and scaling any single voice (as originally named by *Goupillaud et al.* [1984]) $\mathcal{W}[g,\phi_0]\,(b, a = \text{constant})$ of the wavelet transform:

$$\mathcal{W}[g,\phi_0](b,a') = \left(\frac{a'}{a}\right)^{n+\alpha} \mathcal{D}_{a'/a}\mathcal{W}[g,\phi_0](b,a). \tag{6}$$

This analytical property translates into a nice geometrical property since the points where $(\partial^m/\partial b^m)\,\mathcal{W}[g,\phi_0]\,(b,a) = 0$ are unions of straight lines forming a cone-like pattern whose apex is the center of homogeneity of the analyzed function when $a \downarrow 0$. Such lines corresponding to $(\partial/\partial b)\,\mathcal{W}[g,\phi_0]\,(b,a) = 0$ are shown in Figure 2. These lines will hereinafter be referred to as the ridges of the wavelet transform. Along such ridges the magnitude of the wavelet transform varies according to a power law of the form a^α, which provides a simple way to estimate the regularity α of the analyzed homogeneous function (Figure 2) [*Grossmann et al.*, 1987; *Holschneider*, 1988]. A more detailed discussion of this technique and applications to geomagnetic time series can be found in the work of *Alexandrescu et al.* [1995, 1996].

2.2. Harmonic Continuation of Potential Fields and Homogeneous Sources

We now recall the mathematical properties of potential fields that we need in this paper. Consider the following boundary value problem of the harmonic continuation for a field ϕ:

$$\nabla^2\phi(q) = 0,\ \forall q = (x,z) \in \mathbb{R}^n \times \mathbb{R}^+ \tag{7}$$

$$\phi(x, z=0) = \phi_0(x) \tag{8}$$

$$\int_{\mathbb{R}^n} \mathrm{d}x\,|\phi(x, z \geq 0)|^2 < \infty. \tag{9}$$

Here $\phi_0(x)$ is a bounded and square-integrable function, and condition (9) implies that the field $\phi(x,z)$ is uniquely determined by $\phi_0(x)$ and its boundary behavior at infinity. The field ϕ is the harmonic continuation of ϕ_0 from the hyperplane $\mathbb{R}^n$ into the upper half-space defined by $z > 0$. The harmonic continuation can be done through a convolution,

$$\phi(x,z) = (\mathcal{D}_z p * \phi_0)(x) \tag{10}$$

$$\phi(x,z) = \mathcal{W}[p,\phi_0](x,z), \tag{11}$$

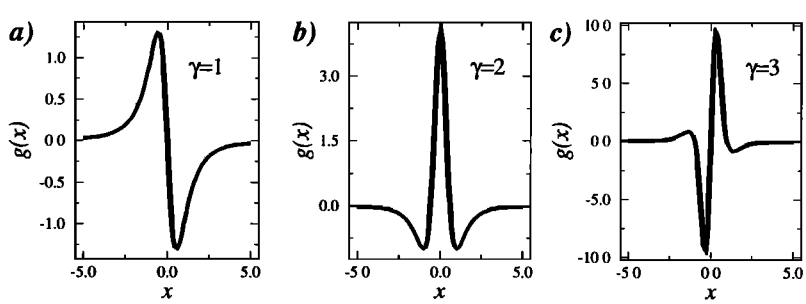

Figure 1. Examples of wavelets g belonging to the class defined by equation (22), including the cases (a) $\gamma = 1$, (b) $\gamma = 2$, and (c) $\gamma = 3$. The cases correspond to an operator $\mathcal{L}$ (see equations (24) and (25)) acting as $\partial/\partial x$, $\partial^2/\partial x^2$, and $\partial^3/\partial x^3$ respectively.

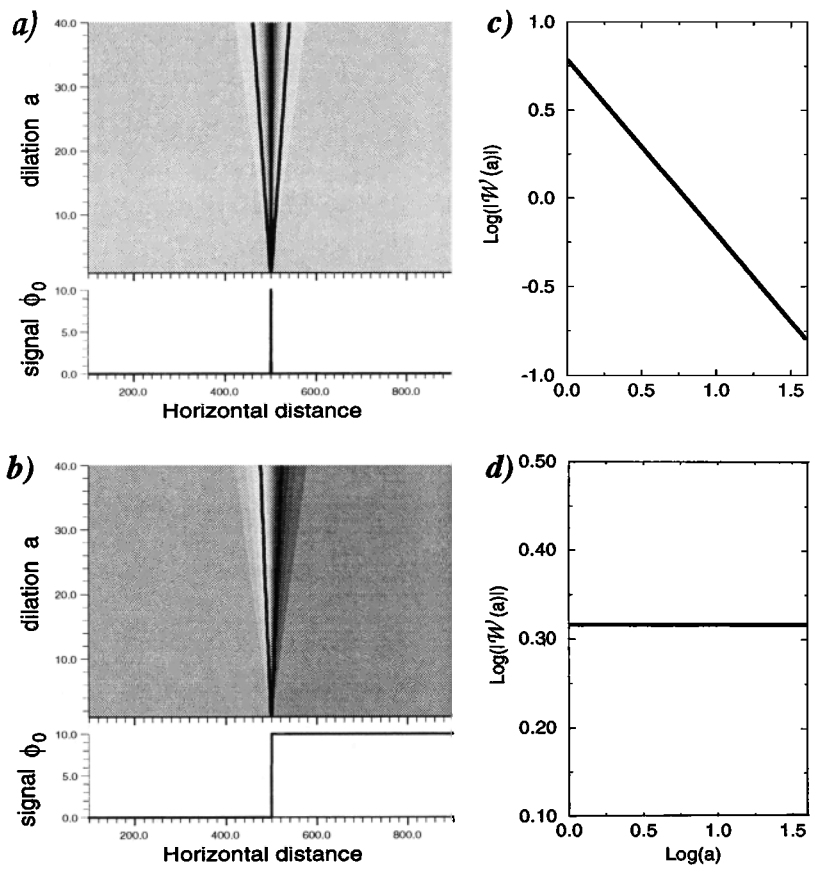

Figure 2. Wavelet transforms of a (a) Dirac distribution with regularity $\alpha = -1$ and a (b) Heaviside distribution with $\alpha = 0$. The grey maps (dark grey levels for negative values and light grey levels for positive values) represent the amplitude (in arbitrary units) of the wavelet transform of the signals shown just below. The analyzing wavelet is shown in Figure 1b. Observe the typical cone-like structure of the wavelet transforms pointing toward the homogeneity center of the analyzed functions. This cone-like geometry can easily be tracked with the ridges (black solid lines) of the wavelet transforms. (c,d) The modulus of the wavelet transform is taken along the ridge and plotted as a function of the dilation a. In this log-log diagram, the modulus of the wavelet transform varies linearly with a slope equal to the regularity α of the analyzed homogeneous function.

where the Poisson kernel is given by

$$p(x) = c_{n+1}\left(1 + |x|^2\right)^{-(n+1)/2} \tag{12}$$

Also, observe that the harmonic continuation may be written under the form of a wavelet transform and that the Poisson kernel verifies the semigroup property,

$$\mathcal{D}_z p * \mathcal{D}_{z'} p = \mathcal{D}_{z+z'} p, \tag{13}$$

which will play a fundamental role in the remainder of this paper.

We shall now specialize our study to the particular class of potential fields produced by homogeneous sources. So, consider now the Poisson equation

$$\nabla^2 \phi(q) = -\sigma(q) \quad q \in \mathbb{R}^{n+1}, \tag{14}$$

where the source term $\sigma(q)$ is assumed to be a homogeneous distribution of degree α (for example, a dipole) with respect to the point $(0, z_\sigma \leq 0)$ and whose support is a subset of the lower half-space $\mathbb{R}^n \times \mathbb{R}^-$. We have

$$\sigma\left(\frac{x}{\lambda}, z\right) = \lambda^{-\alpha}\sigma\left[x, \lambda(z - z_\sigma) + z_\sigma\right], \tag{15}$$

and the potential field corresponding to such a homogeneous source also is homogeneous of degree $\alpha + 2$, i.e.,

$$\phi\left(\frac{x}{\lambda}, z\right) = \lambda^{-\alpha-2}\phi\left[x, \lambda(z - z_\sigma) + z_\sigma\right], \tag{16}$$

or, introducing the measured field $\phi_0(x)$,

$$\mathcal{D}_\lambda \phi_0(x) = \lambda^{-n-\alpha-2}\phi\left[x, (1-\lambda) z_\sigma\right], \tag{17}$$

where the dilation operator acts on the first n variables (i.e., x) only. This last expression shows that for homogeneous potential fields the dilation operator essentially acts like a continuation operator. Indeed, comparing (10) and (17), we obtain the following equivalence:

$$\mathcal{D}_{(1-\lambda)z_\sigma} p * = \lambda^{n+\alpha+2}\mathcal{D}_\lambda. \tag{18}$$

2.3. Wavelet Analysis of Homogeneous Potential Fields

We now use the properties recalled in sections 2.1 and 2.2 to derive the main result of this paper. We begin with the covariance of the wavelet transform (equation (3)) with respect to dilation and the homogeneity of the field ϕ (equation (17)) to obtain the following:

$$\begin{aligned}\mathcal{W}[g,\phi_0](b,a) &= \lambda^n \mathcal{W}[g,\mathcal{D}_\lambda\phi_0](\lambda b,\lambda a)\\ &= \lambda^{-\alpha-2}\mathcal{W}[g,\phi(x,(1-\lambda)z_\sigma)](\lambda b,\lambda a)\end{aligned} \quad (19)$$

Now the harmonic continuation (equation (10)) gives

$$\phi[x,(1-\lambda)z_\sigma] = \left[\mathcal{D}_{(1-\lambda)z_\sigma}p * \phi_0\right](x), \quad (20)$$

which, inserted into (19), reads

$$\mathcal{W}[g,\phi_0](b,a) = \lambda^{-\alpha-2}\left[\left(\mathcal{D}_{(1-\lambda)z_\sigma}p * \mathcal{D}_{\lambda a}\right)g * \phi_0\right](\lambda b). \quad (21)$$

Here we have written the wavelet transform as a convolution product as in (1).

2.4. Wavelets Based on the Poisson Semigroup

We now introduce a new class of wavelets possessing remarkable properties under the Poisson semigroup and which allows a nice simplification of (21) into a form very similar to (5) obtained for homogeneous functions. The wavelets belonging to this class are such that the harmonic continuation acts like a dilation as in (18), i.e.,

$$(\mathcal{D}_a p * \mathcal{D}_{a'})\,g = \left(c\mathcal{D}_{a''}\right)g, \quad (22)$$

where both the scaling factor c and the dilation a'' depend on a, a', and g only. Provided the analyzing wavelet g satisfies (22), (21) simplifies into

$$\begin{aligned}\mathcal{W}[g,\phi_0](b,a) &= \lambda^{-\alpha-2}\left[c\mathcal{D}_{a''}g * \phi_0\right](\lambda b)\\ &= c\lambda^{-\alpha-2}\mathcal{W}[g,\phi_0]\left(\lambda b, a''\right),\end{aligned} \quad (23)$$

which furnishes a relation between the voices of the wavelet transform of the homogeneous field.

A remaining task is to obtain explicit expressions for c and a'' in terms of a, λ, and z_σ. It can be shown [*Moreau et al.*, 1997] that a whole class of wavelet satisfying (22) can be constructed by applying a linear operator $\mathcal{L}$ to the Poisson kernel p, i.e.,

$$g = \mathcal{L}p. \quad (24)$$

We have shown that a sufficient condition to satisfy (22) is that $\mathcal{L}$ be a Fourier multiplier homogeneous of degree γ, i.e., such that

$$\mathcal{L}:\widehat{p}(u) \longmapsto \widehat{l}(u)\,\widehat{p}(u) \quad \widehat{l}(\lambda u) = \lambda^\gamma \widehat{l}(u), \quad (25)$$

where $\widehat{p}(u)$ stands for the Fourier transform of $p(x)$. Several wavelets obtained with the operator $\mathcal{L}$ acting as $\partial/\partial x$, $\partial^2/\partial x^2$, and $\partial^3/\partial x^3$ are shown in Figure 1. Their expressions are

$$g(x) = -(2/\pi)\,x\,(1+x^2)^{-2}, \quad (26)$$

$$g(x) = -(2/\pi)\,(1-3x^2)\,(1+x^2)^{-3}, \quad (27)$$

$$g(x) = (24/\pi)\,(1-x^2)\,(1+x^2)^{-4}, \quad (28)$$

respectively. For this class of wavelets, (23) can be reduced to the following simple form:

$$\mathcal{W}[g,\phi_0](b,a) = \left(\frac{a}{a'}\right)^\gamma \left(\frac{a'-z_\sigma}{a-z_\sigma}\right)^{\gamma-\alpha-2} \mathcal{W}[g,\phi_0]\left(b\frac{a'+z_\sigma}{a+z_\sigma}, a'\right) \quad (29)$$

It can be observed that this expression is very similar to (5) except that the z_σ term is present in both the scaling and dilation factors on the right-hand side. This results in a fundamental difference in the geometrical translation of this equation since, contrary to the case of homogeneous functions for which the cone-like pattern converges on the hyperplane $a = 0$ (Figure 2), the cone-like pattern implicit in (29) converges below this hyperplane at the negative dilation $a = z_\sigma$ (see Figure 3 and the discussion in section 2.5). Indeed, up to the following scaling and change of coordinates,

$$\mathcal{W}[g,\phi_0](b,a) \longrightarrow \left(\frac{1}{a}\right)^\gamma \mathcal{W}[g,\phi_0](b,a) \quad (30)$$

$$a \longrightarrow a - z_\sigma, \quad (31)$$

(29) can be rewritten under a form identical to (6):

$$\mathcal{W}[g,\phi_0](b,a') = \left(\frac{a'}{a}\right)^{-\gamma+\alpha+2} \mathcal{D}_{a'/a}\mathcal{W}[g,\phi_0](b,a). \quad (32)$$

In a way very similar to that which can be done for homogeneous functions, the wavelet transform then allows for a straightforward determination of the regularity α of the source causing the analyzed potential field.

2.5. Synthetic Example

This example illustrates the application of (32) to potential fields created by isolated homogeneous sources. We work in a two-dimensional physical space corresponding to $n = 1$. The first example is shown in Figure 3a and corresponds to the potential of a vertical dipole located at $x = 300$ and $z_\sigma = -20$. This dipolar source can be written as $\sigma(x,z) = (\partial/\partial z)\,\delta(x-300, z+20)$ and has a homogeneity $\alpha = -3$. The example shown in Figure 3b corresponds to a quadrupolar source with a regularity $\alpha = -4$. The wavelet transforms of the fields produced by these sources have been computed with the wavelet shown in Figure 1 ($\gamma = 1$) and have a cone-like structure very similar to the one obtained when analyzing homogeneous functions. However, as already said, the ridges now converge toward the homogeneity center of the source, i.e., below the line $a = 0$. We then observe that the wavelet transform of potential fields caused by homogeneous sources possesses a re-

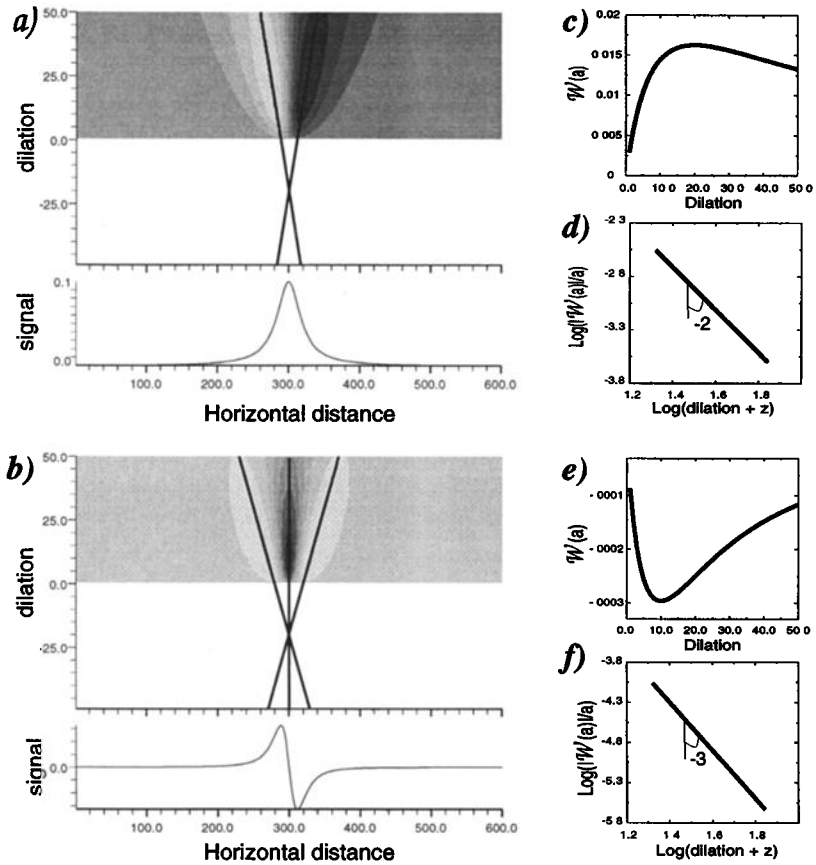

Figure 3. Wavelet transforms of potential fields caused by a (a) vertical dipole and by a (b) quadrupole. The analyzing wavelet is the one shown in Figure 1a. As for pure singularities (see Figure 2), these wavelet transforms also display a cone-like pattern, but it points toward the location of the homogeneity center at a negative dilation corresponding to the depth of the causative source. (c,e) When plotted in a log-log diagram, the amplitude of the wavelet transform along the ridges does not vary linearly. (d,f) Instead, both a change of coordinates and a scaling are necessary to recover the linear variation with a slope equal to the homogeneity of the source term.

markable geometrical property which allows for an easy location, both horizontal and vertical, of the causative sources. The amplitude of the wavelet transforms taken along the ridge does not vary linearly as observed for the ridges of the wavelet transforms of homogeneous functions; instead, a scaling (equation (30)) and a change of coordinates (equation (31)) are necessary to recover a linear law with a slope $\beta = -\gamma + \alpha + 2$.

3. Practical Issues

3.1. Analyzing Noisy Data

We now address the influence of noise in the detection procedure explained above. Suppose that the data $d(x)$ are such that

$$d(x) = \phi_0(x) + \nu(x), \tag{33}$$

where $\nu(x)$ represents the noise present in the data to be analyzed. Of course,

$$\mathcal{W}[g,d](b,a) = \mathcal{W}[g,\phi_0](b,a) + \mathcal{W}[g,\nu](b,a), \tag{34}$$

which shows that the wavelet transform of the data is the sum of a deterministic part $\mathcal{W}[g,\phi_0](b,a)$ with a stochastic process $\mathcal{W}[g,\nu](b,a)$ whose influence depends on the statistical nature of the noise. For instance, if $\nu(x)$ is Gaussian white noise with zero mean and variance σ_ν^2, the linearity of the wavelet transform ensures that $\mathcal{W}[g,\nu](b,a)$ is also Gaussian noise with a variance

$$\begin{aligned}\sigma^2_{\mathcal{W}[g,\nu]}(a) &= \sigma_\nu^2 \int_{-\infty}^{+\infty} (\mathcal{D}_a g)^2(x)\,\mathrm{d}x \\ &= a^{-1}\sigma_\nu^2 \int_{-\infty}^{+\infty} g^2(\xi)\,\mathrm{d}\xi \\ &= a^{-1}\sigma_\nu^2 E_g,\end{aligned} \tag{35}$$

where $E_g = \int_{-\infty}^{+\infty} g^2(\xi)\,\mathrm{d}\xi$ is the energy of the analyzing wavelet. Equation (35) shows that the variance of $\mathcal{W}[g,\nu](b,a)$, which is also the variance of the wavelet transform of the data, varies like a^{-1}. Thus the fluctuations of $\mathcal{W}[g,\nu](b,a)$ decrease like $a^{-1/2}$, and the

wavelet transform at small dilations will be more corrupted by the noise than it is at large dilations. Asymptotically, we expect that

$$\mathcal{W}[g,d](b,a \gg a_c) \simeq \mathcal{W}[g,\phi_0](b,a), \tag{36}$$

and

$$\mathcal{W}[g,d](b,a \ll a_c) \simeq \mathcal{W}[g,\nu](b,a), \tag{37}$$

where a_c is a corner dilation corresponding to a signal-to-noise ratio of the order of 1. This asymptotic behavior can be checked in Figure 4, which represents the wavelet transforms of the same potential fields as those in Figure 3 but corrupted by a Gaussian white noise. We observe that for small dilations the amplitude of the wavelet transform taken along the ridges strongly departs from the linear variation related to the deterministic part of the wavelet transform (after applying the scaling and the translation). This linear variation is preserved at sufficiently large dilations where the stochastic part of the wavelet transform becomes negligible. As can be checked in Figure 4, the corner dilation a_c is well defined, and the slope of the ridge is stable for $a > a_c$. The cone-like pattern is distorted by the stochastic part of the wavelet transform, but as can be observed, this distortion is minimized for the lines of extrema where the signal-to-noise ratio is maximum. This is why these lines remain accurately straight and intersect near the right depth z_σ as long as only the dilations $a > a_c$ are considered. This example shows that the wavelet analysis can be locally adapted with respect to the signal-to-noise ratio depending on the relative amplitude of the analyzed anomalies compared with the noise amplitude. This constitutes an advantage not shared by the Euler deconvolution method.

3.2. Fields Produced by Extended Sources

The analyzed potential fields are always caused by distributed sources which cannot be represented by a single homogeneous source. In such a situation the measured field ϕ_0 can be written as a convolution product,

$$\phi_0(x) = \int_{-\infty}^{0} \mathrm{d}z\,[s(\cdot,z) * G(\cdot,z)](x), \tag{38}$$

where $s(x,z)$ is the source term and $G(x,z)$ is a suitable Green function. The wavelet transform of the field ϕ_0 reads

$$\begin{aligned}\mathcal{W}[g,\phi_0](b,a) &= \left[\mathcal{D}_a g * \int_{-\infty}^{0} s(\cdot,z) * G(\cdot,z)\,\mathrm{d}z\right](b)\\ &= \left[\mathcal{D}_a \mathcal{L} p * \int_{-\infty}^{0} s(\cdot,z) * G(\cdot,z)\,\mathrm{d}z\right](b)\\ &= \left[\mathcal{D}_a L * \mathcal{D}_a p * \int_{-\infty}^{0} s(\cdot,z) * G(\cdot,z)\,\mathrm{d}z\right](b) \end{aligned}\tag{39}$$

where the last line has been obtained by writing the action of the Fourier multiplier $\mathcal{L}$ as the convolution product $L*$. Rearranging the terms and introducing the transformed source distribution

$$s_L(x,z) \equiv [L * s(\cdot,z)](x), \tag{40}$$

we obtain

$$\begin{aligned}&\mathcal{W}[g,\phi_0](b,a) =\\ &\left[\mathcal{D}_a p * \int_{-\infty}^{0} \mathcal{D}_a L * s(\cdot,z) * G(\cdot,z)\,\mathrm{d}z\right](b)\\ &= \left[\mathcal{D}_a p * \int_{-\infty}^{0} a^{\gamma} s_L(\cdot,z) * G(\cdot,z)\,\mathrm{d}z\right](b). \end{aligned}\tag{41}$$

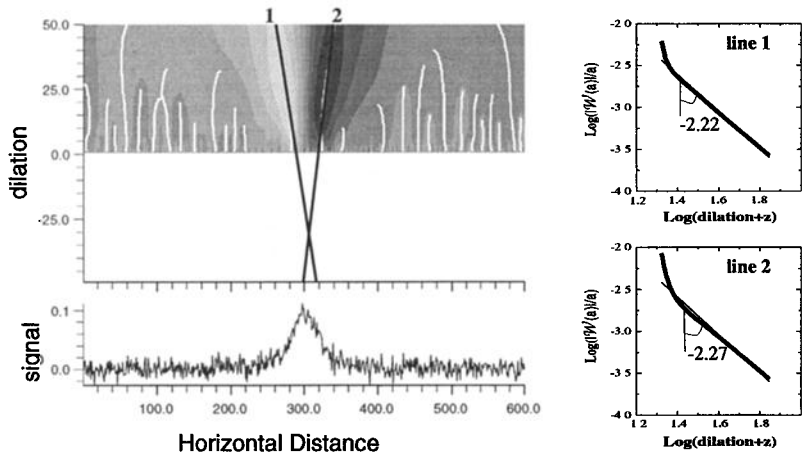

Figure 4. (left) Wavelet transform of the example signal shown in Figure 3a but polluted by Gaussian white noise. Many lines of extrema have appeared owing to this noise, but the two lines (labeled 1 and 2) observed in Figure 3 and corresponding to the deterministic part of the wavelet transform remain unaltered except for small dilations, and they converge toward the right location of the source. (right) When properly scaled, the ridges are accurately straight beyond a well-defined corner dilation.

The source $s_L(x,z)$ produces the transformed potential field

$$\phi_{0,L}(x) = \int_{-\infty}^{0} \mathrm{d}z \left[s_L(\cdot,z) * G(\cdot,z)\right](x), \qquad (42)$$

and we finally obtain the following expression for the wavelet transform of the measured field ϕ_0:

$$\mathcal{W}[g,\phi_0](b,a) = a^{\gamma}\left[\mathcal{D}_a p * \phi_{0,L}\right](b). \qquad (43)$$

Comparing this equation with (10), we observe that the wavelet transform of ϕ_0 is the harmonic continuation $\phi_L(x,a)$ of the field $\phi_{0,L}(x)$ caused by the transformed source $s_L(x,z)$.

3.3. Choosing the Analyzing Wavelet

We now address the question of the choice of the analyzing wavelet g. In the case of a distributed source $s(x,z)$, the analyzing wavelet plays an important role since it controls the properties of the transformed source distribution $s_L(x,z)$. In practice, we want the analyzing wavelet to produce a transformed source composed of scattered homogeneous sources in order to locally apply the theory developed in section 2. However, recall that the operator $\mathcal{L}$ which defines the analyzing wavelet acts through a convolution over the x variable only (see equation (40)) and that the vertical dimension z is not directly accessible. From the point of view of inverse problem theory, this translates into the fact that all sources $s(z)$ independent of the horizontal variable x belong to the null space of the wavelet transform in the sense that such sources produce constant potential fields with a vanishing wavelet transform. This implies that the wavelet transform only enables the detection of horizontal variations in the source $s(x,z)$. For the frequently encountered situation where the source is smooth almost everywhere and possesses sharp variations occupying a sparse subset of $\mathbb{R}^n \times \mathbb{R}^-$ (e.g., juxtaposition of homogeneous blocks), the transformed source $s_L(x,z)$ takes large values only in the neighborhood of the horizontal sharp variations.

Figure 5 shows the example of a prismatic source with a constant vertical magnetization inside the prism and no magnetization elsewhere. The left edge of the prism is vertical, and the right one is inclined rightward (45°). The depth to top equals 20, and the depth to bottom equals 80 units of length. The wavelet transform computed with $g(x) = (\mathrm{d}/\mathrm{d}x)\,p(x)$ ($\gamma = 1$) (Figure 5, top) takes large values above the lateral edges of the prism and small ones above the horizontal edges. The transformed source $s_L(x,z) = (\mathrm{d}/\mathrm{d}x)\,s(x,z)$ is physically made of two lines of dipolar sources located on the lateral edges of the prism. Since there is only one line of maxima above each edge, the depth of the source cannot be determined by looking for the intersection of the lines of maxima as in the preceding examples. Instead, the depth can only be determined by looking for the values of z_σ at which the ridges become linear under

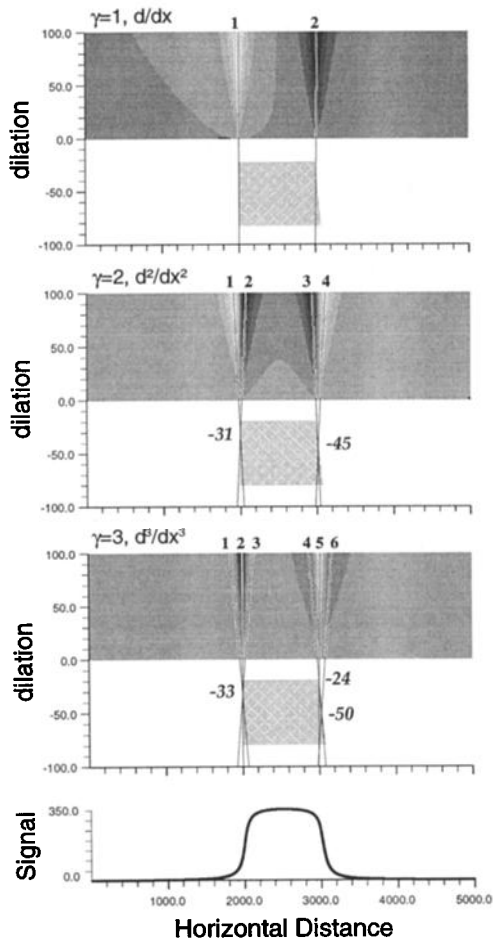

Figure 5. Wavelet transforms of the potential field produced by a prismatic body with a vertical left edge and an inclined (45°) right one. The depth to top of the prism equals 20 units length and the depth to bottom equals 80 units length. The prism has a constant vertical magnetization. These wavelet transforms have been obtained with the three wavelets shown in Figure 1 and corresponding to different operators $\mathcal{L}$ (see text for a detailed discussion).

the scaling defined by (30) and (31). Since γ is known, the only variable parameter is z_σ, which, in practice, is determined by spanning an a priori depth interval and by quantifying the linear character of the transformed experimental ridge by fitting (in the least squares sense in the present study) a polynomial of degree 1. This is shown in Figure 6 (middle) where the L_2 misfit curves possess a single minimum. The slope β of the fitted lines is also given in Figure 6 (top). We observe that $\beta \simeq -1$ so that $\alpha \simeq -2$, which is compatible with the fact that the transformed source is a line of dipoles, i.e., a finite integral of dipoles along the edges of the prism. The best-fitting depths are 37 and 47 units of length for the left and right edge, respectively. The ridges rescaled according to these values are shown in Figure 6 (bottom) and appear accurately linear. The depth obtained for the vertical edge falls near the upper third of the

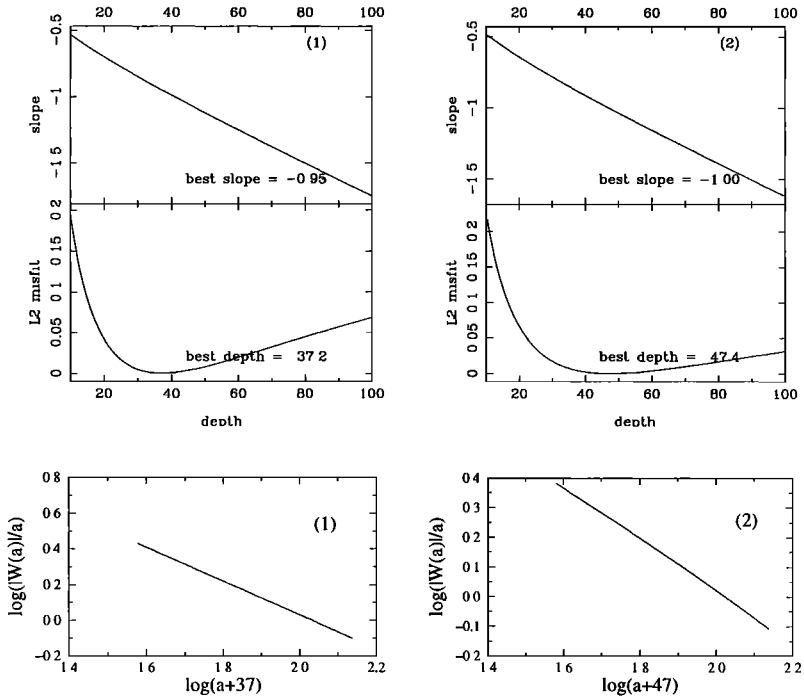

Figure 6. Results of the inversion of the ridges extracted from the wavelet transform displayed in the top of Figure 5 and obtained with the $L = \mathrm{d/dx}$ operator producing the $\gamma = 1$ wavelet shown in Figure 1a. (top) Corresponding slope β of the least squares line is adjusted for each value of z_σ. (middle) Misfit between the least squares line and the rescaled ridge is shown as a function of the parameter z_σ. (bottom) Ridges were rescaled with the best z_σ obtained by the least squares analysis.

edge, while the depth derived for the inclined edge falls near the barycenter of the edge.

The wavelet transform shown in Figure 5 (middle) corresponds to the analyzing wavelet $g(x) = (\mathrm{d}^2/\mathrm{d}x^2)\, p(x)$ ($\gamma = 2$), and the transformed source corresponds to two lines of quadrupolar sources located on the lateral edges of the prism. Two lines of extrema exist above each edge, and as for the preceding example, the misfit curves possess a single minimum. The depths found for the left vertical edge are very similar, 33 and 30 for lines 1 and 2, respectively, while those for the right inclined edge are quite different: 32 for line 3 located near the shallow end of the edge and 64 for line 4 located toward the deep end of the edge. The depth obtained from the intersection of the ridges (see Figure 5) equals 31 for the left edge and is consistent with the results obtained from the least squares analysis just discussed. The depth obtained for the right edge roughly falls just between the two depths obtained by analyzing the two ridges independently. The ridges rescaled according to the optimal depths are found to be accurately linear as in the preceeding example. The slopes for lines 1, 2, and 3 fall near -1.75, and the slope for line 4 is larger (-2.14). These values fall near the theoretical value -2 corresponding to a pure dipolar source, and they are compatible with the fact that the transformed sources are finite integrals of quadrupolar sources.

The wavelet transform shown in Figure 5 (bottom) corresponds to the analyzing wavelet $g(x) = \mathrm{d}^3/\mathrm{d}x^3 p(x)$ ($\gamma = 3$). The transformed source corresponds to two lines of octupolar sources located on the lateral edges of the prism, and now three lines of extrema converge above each lateral edge of the prism (Figure 5). Lines 1, 2, and 3 form a symmetrical pattern above the left edge of the prism and converge toward a common point located at a depth of 33 units of length. The three lines associated with the right edge are not symmetrical and do not converge toward a common point. Instead, lines 4 and 5 converge at a depth of 24 units while the rightmost line cuts the two companion lines at greater depths (50 and 75). The depths obtained for each of the three ridges located on the left edge are quite similar: 21.5, 23.9, and 21.5 for lines 1, 2, and 3, respectively. The best β are also very similar: -2.29, -2.50, and -2.29 for lines 1, 2, and 3. As in the former two examples, the rescaled ridges are linear. The depths obtained by analyzing the three ridges located above the right edge are consistent with the one derived from the intersection of the lines of extrema (see Figure 5). Lines 4 and 5 have corresponding depths equal to 17.9 and 21.5, respectively, and they fall near the shallow end of the right edge, while the depth for line 6 equals 75.2 and falls near the deep end of the edge.

Although the theory derived for homogeneous sources

is not directly applicable to extended sources, the three examples presented above show that the wavelet transform yet enables us to locate, both horizontally and vertically, the sharp edges of extended sources. The depths obtained with the ridges fall within the depth range of the detected edges, and for the vertical edge these depths correspond to the upper part of the source. Furthermore, the larger γ, the shallower the depths. This can be explained by the fact that the transformed source is made of multipoles of larger order when γ is larger and that the resulting potential field is less controlled by the deep parts of the source. For the inclined edge, the depth obtained with the $\gamma = 1$ wavelet falls near the barycenter of the edge, but for larger γ the situation becomes more complicated since the higher order of derivation eventually allows the separation of the extremities of the edge as is particularly clear for the $\gamma = 3$ example. However, it must be recalled that the $\gamma = 3$ analyzing wavelet amplifies the noise present in the data and that the small dilations are more corrupted than those for the $\gamma = 1$ case.

4. Field Example

We now briefly discuss an application of the wavelet transform to a near-surface magnetic survey where the two-dimensional approximation is valid. This enables a much easier representation of the results than that in a full three-dimensional geometry. In this example the data were acquired in a small area over a steel pipe carrying hot water across our university campus. Since the location of the pipe is well known, this example provides a tight control of the method. The measurements were made with a magnetometer operating at a sampling interval of 0.25 m. The total duration of the survey was less than a quarter of an hour so that no diurnal correction was needed. The intensity of the magnetic field recorded along tracks perpendicular to the pipes is shown in Figure 7 (bottom).

The wavelet transform of the data is also shown in Figure 7 (top) and was computed with the analyzing wavelet shown in Figure 1a. The analysis of the ridges associated with these two lines (Figure 8) gives a depth of 5.8 and 5.3 unit lengths, i.e., 1.5 and 1.3 m. These values fully agree with the value (1.6 m) given on the campus map. The best slopes β equal -2.65 and -2.85 and give source homogeneities α of the same value because one must add one more derivative to γ since we analyze a magnetic field instead of a potential. The α values obtained fall very near the theoretical value (-3.0) corresponding to a pure dipolar source. The ridges rescaled according to the best depths found are shown in Figure 8 (bottom). One can observe that the rescaled ridges are accurately linear on the whole dilation interval and that no noise effect is apparent in the small dilation part (for comparison, refer to Figure 4 and to section 3.1 concerning the effects of noise).

5. Conclusion

The method presented in this study belongs to the class of the processing methods which transfer the information content of the data into an auxiliary space. Here the target space is the continuous wavelet transform domain where the local homogeneity of the analyzed field can be easily obtained. We have shown that the lines of extrema of the wavelet transform provide a sufficient subset containing the relevant information necessary to recover the main parameter of the homogeneous causative sources (depth, horizontal location,

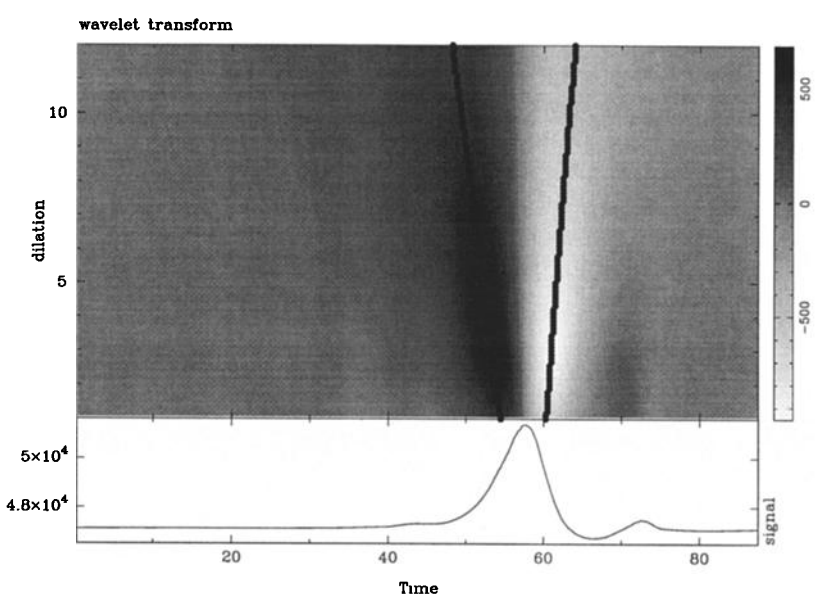

Figure 7. (top) Wavelet transform and (bottom) magnetic profile displayed for the analyzing wavelet shown in Figure 1a. The analyzing wavelet was obtained with the $L = \mathrm{d}/\mathrm{dx}$ operator.

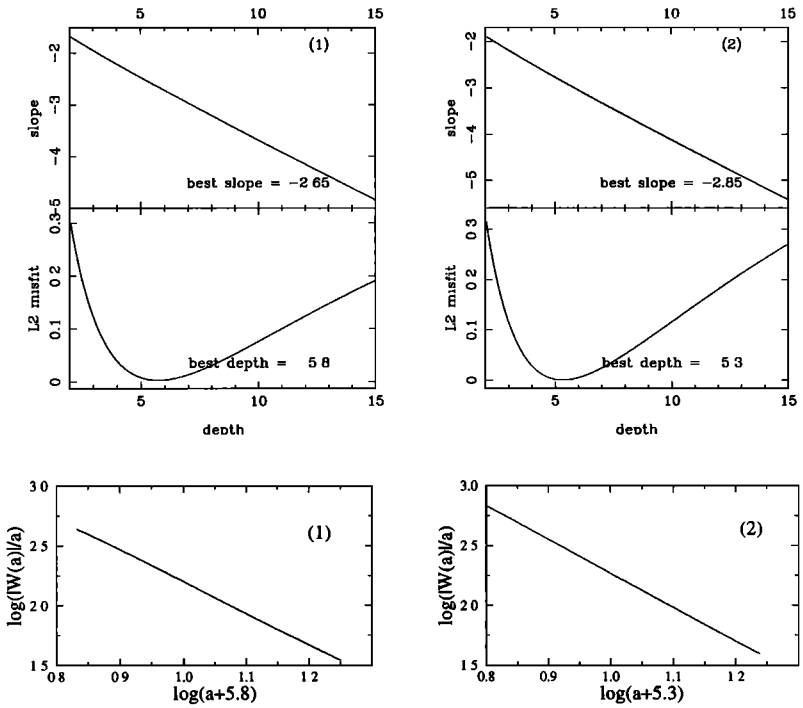

Figure 8. (top and middle) Results (see caption of Figure 6 for details) of the inversion of the ridges extracted from the wavelet transform displayed in Figure 7 and obtained with the $L = \mathrm{d}/\mathrm{dx}$ operator (analyzing wavelet in Figure 1a). (bottom) Observe that the rescaled ridges are linear on the whole dilation interval and that no noise effect is visible at small dilations.

strength, and degree of homogeneity). The comprehensive theory available for homogeneous sources is useful to understand the wavelet transforms of fields produced by extended sources, for which the homogeneity hypothesis is not valid. For such sources the choice of the analyzing wavelet is important since it allows for a segmentation of the initial extended source into a small number of quasi-homogeneous sources. In the case of extended sources the wavelet transform allows a local analysis of the measured field. The synthetic examples show that the noise can efficiently be taken into account and in a nonstationary way. The examples concerning an extended source show that the wavelet analysis allows a local study of the structural elements (edge, corner, etc.) of the whole source. The application of the method to a simple field example further demonstrates the easy use of this technique, which can easily be implemented on portable computers and operated by field practitioners.

Acknowledgments. This paper benefited from comments made by Associate Editor Patrick Taylor, Richard Hansen, and an anonymous reviewer. We also had numerous discussions with our colleagues Alex Grossmann, Jean Morlet, and Pascal Sailhac. The present study has been granted by the Centre National de la Recherche Scientifique (CNRS-INSU) via ATP Tomographie.

References

Alexandrescu, M., D. Gibert, G. Hulot, J.-L. Le Mouël, and G. Saracco, Detection of geomagnetic jerks using wavelet analysis, *J. Geophys. Res.*, *100*, 12557-12572, 1995.

Alexandrescu, M., D. Gibert, G. Hulot, J.-L. Le Mouël, and G. Saracco, Worldwide wavelet analysis of geomagnetic jerks, *J. Geophys. Res.*, *101*, 21975-21994, 1996.

Blakely, R.J., *Potential Theory in Gravity and Magnetic Applications*, Cambridge Univ. Press, New York, 1995.

Gibert, D., and A. Galdéano, A computer program to perform transformations of gravimetric and aeromagnetic surveys, *Comput. Geosci.*, *11*, 553-588, 1985.

Goupillaud, P., A. Grossmann, and J. Morlet, Cycle-octave and related transforms in seismic signal analysis, *Geoexploration*, *23*, 85-102, 1984.

Green, A.G., Magnetic profile analysis, *Geophys. J. R. Astron. Soc.*, *30*, 393-403, 1972.

Grossmann, A., M. Holschneider, R. Kronland-Martinet, and J. Morlet, Detection of abrupt changes in sound signals with the help of wavelet transforms, in *Advances in Electronics and Electron Physics*, vol. 19, pp. 289-306, Academic, San Diego, Calif., 1987.

Holschneider, M., On the wavelet transformation of fractal objects, *J. Stat. Phys.*, *50*, 953-993, 1988.

Holschneider, M., *Wavelets: An Analysis Tool*, Clarendon, Oxford, England, 1995.

Hornby, P., F. Boschetti, and F.G. Horowitz, Analysis of potential field data in the wavelet domain, *Geophys. J. Int.*, in press, 1999.

Moreau, F , D. Gibert, M. Holschneider, and G. Saracco, Wavelet analysis of potential fields, *Inverse Probl.*, *13*, 165-178, 1997.

Parker, R.L., *Geophysical Inverse Theory*, Princeton Univ. Press, Princeton, N. J., 1994.

Sowerbutts, W.T.C., Magnetic mapping of the Butterton Dyke: An example of detailed geophysical surveying, *J. Geol. Soc. London*, *144*, 29-33, 1987.

Spector, A., and F.S. Grant, Statistical models for interpreting aeromagnetic data, *Geophysics*, *35*, 293-302, 1970.

Thompson, D.T., EULDPH: A new technique for making computer-assisted depth estimates from magnetic data, *Geophysics*, *47*, 31-37, 1982.

D. Gibert, F. Moreau, and G. Saracco, Géosciences Rennes, Université de Rennes 1, Bât. 15 Campus de Beaulieu, 35042 Rennes cedex, France. (e-mail: gibert@univ-rennes1.fr; moreau@univ-rennes1.fr; ginet@univ-rennes1.fr)

M. Holschneider, Centre de Physique Théorique, CNRS Luminy, Case 907, 13288 Marseille, France. (e-mail: hols@cpt.univ-mrs.fr)

(Received July 21, 1998; revised October 19, 1998; accepted November 30, 1998.)